

Temperature-dependent magnetotransport properties of $CoFe_2O_4$/Pt heterostructure

Haomang He(何浩茫), Ruijie Xu(徐睿劼), Anke Song(宋安柯), Zhongqiang Chen(陈中强), and Xuefeng Wang(王学锋)

Citation: Chin. Phys. B, 2026, 35 (**1**): 017502. DOI: 10.1088/1674-1056/ae181c
http://cpb.iphy.ac.cn; http://iopscience.iop.org/cpb

What follows is a list of articles you may be interested in

Induced magneto-conductivity in a two-node Weyl semimetal under Gaussian random disorder

Chuanxiong Xu(徐川雄), Haoping Yu(于昊平), Mei Zhou(周梅), and Xuanting Ji(吉轩廷)
Chin. Phys. B, 2024, 33 (**9**): 097502. DOI: 10.1088/1674-1056/ad59fc

Localization effect in single crystal of $RuAs_2$

Zhe-Kai Yi(易哲铠), Qi Liu(刘琪), Shuang-Kui Guang(光双魁), Sheng Xu(徐升), Xiao-Yu Yue(岳小宇), Hui Liang(梁慧), Na Li(李娜), Ying Zhou(周颖), Dan-Dan Wu(吴丹丹), Yan Sun(孙燕), Qiu-Ju Li(李秋菊), Peng Cheng(程鹏), Tian-Long Xia(夏天龙), Xue-Feng Sun(孙学峰), and Yi-Yan Wang(王义炎)
Chin. Phys. B, 2024, 33 (**4**): 047501. DOI: 10.1088/1674-1056/ad23d9

Topological magnetotransport and electrical switching of sputtered antiferromagnetic $Ir_{20}Mn_{80}$

Danrong Xiong(熊丹荣), Yuhao Jiang(蒋宇昊), Daoqian Zhu(朱道乾), Ao Du(杜奥), Zongxia Guo(郭宗夏), Shiyang Lu(卢世阳), Chunxu Wang(王春旭), Qingtao Xia(夏清涛), Dapeng Zhu(朱大鹏), and Weisheng Zhao(赵巍胜)
Chin. Phys. B, 2023, 32 (**5**): 057501. DOI: 10.1088/1674-1056/acb9ec

Weak localization in disordered spin-1 chiral fermions

Shaopeng Miao(苗少鹏), Daifeng Tu(涂岱峰), and Jianhui Zhou(周建辉)
Chin. Phys. B, 2023, 32 (**1**): 017502. DOI: 10.1088/1674-1056/ac720b

Magnetic field enhanced single particle tunneling in MoS_2-superconductor vertical Josephson junction

Wen-Zheng Xu(徐文正), Lai-Xiang Qin(秦来香), Xing-Guo Ye(叶兴国), Fang Lin(林芳), Da-Peng Yu(俞大鹏), Zhi-Min Liao(廖志敏)
Chin. Phys. B, 2020, 29 (**5**): 057502. DOI: 10.1088/1674-1056/ab8209

RAPID COMMUNICATION

Temperature-dependent magnetotransport properties of $CoFe_2O_4$/Pt heterostructure

Haomang He(何浩茫), Ruijie Xu(徐睿劼), Anke Song(宋安柯), Zhongqiang Chen(陈中强), and Xuefeng Wang(王学锋)†

State Key Laboratory of Spintronics, Jiangsu Provincial Key Laboratory of Advanced Photonic and Electronic Materials, School of Electronic Science and Engineering, Collaborative Innovation Center of Advanced Microstructures, Nanjing University, Nanjing 210093, *China*

(Received 1 September 2025; revised manuscript received 11 October 2025; accepted manuscript online 28 October 2025)

We report on the growth of $CoFe_2O_4$/Pt heterostructure and their magnetotransport properties. The magnetoresistance under high magnetic fields exhibits a sign change when the temperature increases from 5 K to 10 K. The anomalous Hall resistance decreases as the temperature increases. Furthermore, angle-dependent magnetoresistance indicates that the observed magnetotransport behaviors originate from the competition between the spin Hall magnetoresistance and magnetic proximity effect.

Keywords: magnetotransport, magnetoresistance, anomalous Hall effect, $CoFe_2O_4$/Pt heterostructure, magnetic proximity effect

PACS: 75.30.Ds, 76.50.+g, 31.15.aq

DOI: 10.1088/1674-1056/ae181c **CSTR:** 32038.14.CPB.ae181c

1. Introduction

Spin transport, a core research area in condensed matter physics and spintronics, refers to the propagation and interaction of quantum spin states in materials. It focuses on the generation, manipulation, transmission, and detection of spin currents, which induces intriguing phenomena including the spin Seebeck effect, spin pumping effect, Rashba–Edlstein effect, and spin Hall effect (SHE).[1–4] Ferromagnetic insulator (FMI)/heavy metal (HM) heterostructures serve as excellent experimental platforms for the creation and manipulation of spin currents, with the advantage of avoiding Joule heating losses.[5,6] Thus, the FMI/HM heterostructures are highly desirable for exploring magnetotransport properties.

Recently, FMI/HM heterostructures have advanced rapidly with the discovery of a series of unconventional effects due to their low damping, efficient spin-charge conversion, and low Joule heat dissipation.[7–11] For instance, the spin Hall magnetoresistance (SMR) is observed in the $Y_3Fe_5O_{12}$ (YIG)/Pt heterostructure, which is a non-equilibrium proximity phenomenon induced by the concerted action of the SHE and inverse spin Hall effect (ISHE).[12,13] The spin-current-induced switching driven by the charge current is also observed in a vertically magnetized $Tm_3Fe_5O_{12}$/Pt heterostructure.[14] Additionally, the spin-polarized conduction electrons propagate between two magnetic layers in high-quality YIG/Au/YIG structures, which has opened a new class of valve structures beyond the conventional spin valves.[15] These explorations have paved the way for developing ultralow-dissipation spintronic devices based on FMI/HM systems.

$CoFe_2O_4$ (CFO) is a ferrimagnetic insulator with a cubic inverse spinel structure, which has been widely applied in high-frequency devices with the advantages of its excellent magnetic anisotropy (uniaxial anisotropy energy $K_u = 3 \times 10^6$ erg/cm^3),[16] high saturation magnetization ($\sim$19 μ_B/u.c. at 10 K),[17] good microwave absorption properties (~ -55 dB at 9.25 GHz)[18] and high Curie temperature ($\sim$ 843 K).[19] Competing magnetic interactions in the spinel lattice induce distinct magnetic behaviors in CFO with different crystal orientations, and the Co^{2+} ions in CFO contribute to enhanced magnetic anisotropy.[20–22] The insulating property of CFO renders it challenging to study its spin transport property via electrical methods. Therefore, the approach of constructing CFO/HM (e.g., Pt) heterostructure and utilizing the electrical properties of HMs to reflect the spin characteristics in CFO has attracted considerable attention.[20,23,24] CFO/Pt offers an alternative platform for investigating unique magnetotransport properties besides the traditional YIG/Pt system. In fact, the magnetotransport properties (e.g., magnetoresistance (MR) and Hall resistance (R_{xy})) of CFO/Pt may exhibit different behaviors due to the influence of magnetic proximity effect (MPE) and SMR. To distinguish between these two effects, the key point lies in determining whether local magnetic moments or spin polarization are generated in the adjacent metal layer, which has remained a highly controversial issue.[25–27]

In this work, we investigate the magnetotransport proper-

†Corresponding author. E-mail: xfwang@nju.edu.cn

© 2026 Chinese Physical Society and IOP Publishing Ltd. All rights, including for text and data mining, AI training, and similar technologies, are reserved.

ties in a CFO/Pt heterostructure at low temperatures. The MR under high magnetic field features a sign change characteristic as the temperature increases, in contrast with the decreasing characteristic of anomalous Hall resistance ($R_{\rm AHE}$). The angle-dependent magnetoresistance (ADMR) measurements are carried out to analyze the contributions of SMR and MPE to the magnetotransport properties at different temperatures.

2. Experimental details

High-quality 40-nm-thick CFO film was epitaxially grown on (001)-oriented $MgAl_2O_4$ (MAO) substrate via pulsed laser deposition (PLD) technology. A 248 nm KrF excimer laser with a fluence of 1.8 J/cm^2 and a repetition rate of 2 Hz was utilized to ablate a stoichiometric polycrystalline CFO target, which was synthesized via solid-state reaction. Prior to film growth, the substrate was sequentially ultrasonically cleaned in acetone, ethanol, and deionized water, followed by drying in nitrogen gas. During the PLD growth process, the substrate was maintained at 600 °C, with the growth oxygen pressure controlled at 1×10^{-3} mbar. After the CFO deposition was completed, the film was slowly cooled to room temperature under the same oxygen pressure to preserve its crystalline quality. For the CFO/Pt heterostructure sample, following the aforementioned CFO film preparation procedures, a 5-nm-thick Pt layer was deposited *ex-situ* via magnetron sputtering.

The crystalline structure of the CFO film was determined by θ–2θ x-ray diffraction (XRD) using Cu K_α radiation (λ = 1.5418 Å, Bruker D8 Discover). The surface morphology of the CFO sample was characterized by atomic force microscopy (AFM) (SOLVER-P47, NT-MDT) in tapping mode over an area of 1×1 μm^2.

The x-ray absorption spectroscopy (XAS) and x-ray magnetic circular dichroism (XMCD) spectroscopy at the Fe and Co $L_{2,3}$ absorption edges were performed on Beamline BL-07U, Shanghai, China. Oppositely circular polarized x-rays with 100% polarization degree were used successively to resolve XMCD signals from Fe and Co at 6 T. XAS was obtained in total electron yield (TEY) mode at 20 K. The escape depth ($\lambda_{\rm e}$) of photoelectrons was $\sim$ 5 nm.

The MR and R_{xy} of the CFO/Pt film were measured in a standard Hall-bar geometry using a cryogen free measurement system (CFMS-12T, Cryogenic). For ADMR measurement, both longitudinal resistance (R_{xx}) and R_{xy} were acquired via β-angle and γ-angle scans, respectively, with the magnetic field magnitude fixed at 9 T and its direction rotated during the scanning process.

3. Results and discussion

Bulk CFO is crystallized in the ideal cubic inverse spinel structure (space group #227, Fd-3m) with a lattice constant of a = 8.396 Å (Fig. 1(a)). The XRD spectrum of the CFO film is shown in the main panel of Fig. 1(b). For the CFO film deposited on the (00l)-oriented MAO substrate, only (00l) diffraction peaks are observed, indicating that the as-prepared film is highly epitaxial. The inset of Fig. 1(b) presents an enlarged view of the 2θ range from 40° to 46°. The lattice constants of CFO and MAO are 8.29 Å and 8.08 Å, respectively. The surface morphology of the CFO film is shown in Fig. 1(c). The root mean square (RMS) roughness is measured to be 0.225 nm over a scanned area of 1×1 μm^2. Such a smooth surface not only minimizes interfacial disorder between CFO and Pt, but also ensures the accuracy of subsequent magnetotransport measurements.

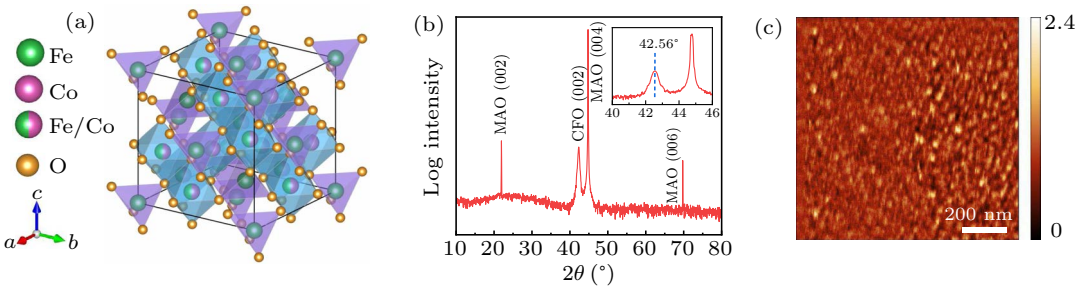


Fig. 1. Surface morphology and structural characterizations of CFO thin films. (a) Schematic diagram of the crystal structure of CFO. (b) θ–2θ x-ray diffraction patterns for the CFO film grown on (001) $MgAl_2O_4$ substrate. Inset in (b) shows the diffraction fringes near the substrate peak (40°–46°). (c) AFM morphology of a 40-nm-thick CFO film.

Figure 2(a) presents a schematic illustration of the inverse spinel structure of CFO and the experimental configuration for XMCD measurements. Figures 2(b) and 2(c) show the XAS spectra (acquired in TEY mode) and XMCD spectra near the Fe and Co $L_{2,3}$ edges of the CFO/Pt sample at 20 K. The magnetic field of 6 T is applied parallel to the direction of the circularly polarized x-ray beam incident on the sample surface. From the perspective of electronic orbital states, Fe^{3+} ions have a $3d^5$ electron configuration, while Co^{2+} ions exhibit a $3d^7$ electron configuration. CFO can crystallize in either a normal spinel or inverse spinel structures. In both cases, O^{2-} form a face-centered cubic (fcc) lattice, with Co^{2+} and Fe^{3+} occupying tetrahedral ($T_{\rm d}$) or octahedral ($O_{\rm h}$) interstitial sites. Specifically, a normal spinel structure is charac-

terized by Co^{2+} occupying T_d sites and Fe^{3+} occupying O_h sites. In contrast, an inverse spinel structure features Co^{2+} and half of the Fe^{3+} in O_h sites, with the remaining half of the Fe^{3+} in T_d sites, where spins of ions in different sites are antiparallel.[26,28,29] The Fe L_3-edge XMCD spectrum exhibits two positive peaks (at $\sim$ 706 eV and $\sim$ 708 eV) and one negative peak (at $\sim$ 707 eV), which correspond to Fe^{3+} occupying T_d and O_h sites. The Co L_3-edge XMCD spectrum shows only one positive peak (at $\sim$ 777 eV), indicating that Co^{2+} ions are exclusively located in O_h sites. No obvious XMCD signals are observed at the Fe and Co L_2 edges. Typically, the intensity ratio of the L_3-edge to L_2-edge XMCD signals for the same element is approximately 2:1. The absence of distinct L_2-edge signals here may be attributed to two factors: first, Fe^{3+} ions primarily contribute to spin magnetic moments, and their orbital magnetic moments are easily quenched in the strong crystal field of T_d sites; second, although Co^{2+} ions have strong spin–orbit coupling (SOC), their orbital magnetic moments are suppressed in the strong crystal field of O_h sites due to high symmetry. Collectively, these results confirm that the CFO in the heterostructure adopts an inverse spinel structure, and the strong crystal field in T_d/O_h sites accounts for the suppressed L_2-edge XMCD signals.[30]

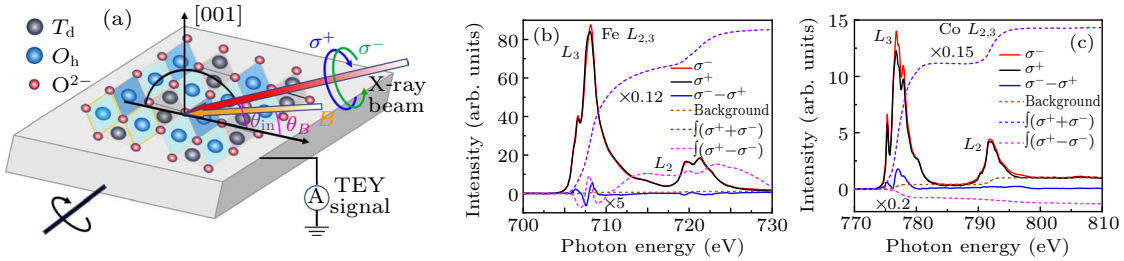


Fig. 2. XMCD measurement. (a) Schematic of the structure of CFO inverse spinel crystal and XMCD experimental setup. Gray and blue represent metal cations at T_d and O_h sites respectively, while the oxygen ions are labeled in red. The magnetic moments of cations at T_d and O_h sites are coupled antiferromagnetically with each other. A circularly polarized x-ray beam was irradiated on the cleaved (001) plane. $\theta_{in}(\theta_B)$ is an angle between (001) plane and x-ray beam (magnetic field). (b) and (c) The XAS (red and black solid lines) and XMCD (blue solid lines) of Fe $L_{2,3}$ and Co $L_{2,3}$, respectively, as well as the background (brown dashed lines)-subtracted integrated curves (purple and pink dashed lines).

Furthermore, to conduct a more detailed analysis of the atomic magnetic moments, background functions and integral curves are fitted to the spectra in the Figs. 2(b) and 2(c). The background is subtracted using a two-step-like function combined with an error function:[31]

$$\begin{aligned}\text{step}(E) = {} & xH_L \times \left[0.5 + 0.5\,\text{erf}\left(\frac{E - P_{L_3}}{\Gamma_G(L_3)\sqrt{\ln 2}}\right)\right] \\ & + (1-x)H_L \times \left[0.5 + 0.5\,\text{erf}\left(\frac{E - P_{L_2}}{\Gamma_G(L_2)\sqrt{\ln 2}}\right)\right], \quad (1)\end{aligned}$$

where H_L is the total height of the steps, x is the proportion of the height of the L_3 step to the total height, P is the absorption peak, and Γ_G is the half-width of the step. The values of $\Gamma_G(L_2)$ and $\Gamma_G(L_3)$ are both set to 1.25.

The orbital magnetic moment (m_{orb}) and the spin magnetic moment (m_{spin}) of Co and Fe are calculated using the XMCD sum rules[32]

$$m_{orb} = -\frac{4\int_{L_2+L_3}(\sigma^+ - \sigma^-)\,dE}{3\int_{L_2+L_3}(\sigma^+ + \sigma^-)\,dE} \times (10 - n_{3d}), \quad (2)$$

$$\begin{aligned}m_{spin} = {} & -\frac{6\int_{L_3}(\sigma^+ - \sigma^-)\,dE - 4\int_{L_2+L_3}(\sigma^+ - \sigma^-)\,dE}{\int_{L_2+L_3}(\sigma^+ + \sigma^-)\,dE} \\ & \times (10 - n_{3d}) \times \left(1 + \frac{7\langle T_z\rangle}{2\langle S_z\rangle}\right)^{-1}, \quad (3)\end{aligned}$$

where σ^- (σ^+) denotes the absorption spectrum for left (right) circularly polarized light after correction for the incident light intensity. The integration is performed using the L_2 and L_3 absorption edges as the integral limits. $\langle T_z\rangle$ represents the expectation value of the magnetic dipole operator. In Hartree atomic units, $\langle S_z\rangle \approx (1/2)m_{spin}$. Theoretical calculations indicate that the ratio $\langle T_z\rangle/\langle S_z\rangle$ is approximately -0.38% for body-centered cubic (bcc) Fe and -0.26% for hexagonal close-packed (hcp) Co.[33] This term can thus be neglected when calculating m_{spin}. n_{3d} refers to the number of 3d orbital electrons. For this work, we adopt values of 6.61 (for Fe) and 7.51 (for Co), which are averages of the values reported in theoretical studies.[34] Using Eqs. (2) and (3), the m_{orb} and m_{spin} of Co are calculated to be 0.231 and 0.015, respectively; for Fe, these values are 0.004 and 0.041, respectively. Compared with results from the literature,[33,34] the calculated magnetic moments in this paper are smaller. This discrepancy arises from the presence of the Pt layer on the CFO film, which modifies the penetration depth of the x-ray beam.

To further explore the spin dynamics behavior in the CFO/Pt heterostructure, we performed the magnetotransport measurement over the temperature range from 5 K to 50 K (Figs. 3(a) and 3(c)). The MR at 5 K exhibits a positive quadratic dependence consistent with Kohler's law $\left(\frac{\rho(B)}{\rho(0)} = f\left(\frac{B}{\rho(0)}\right)^2\right)$ under high magnetic fields (> 2 T), while it becomes negative under low fields (< 2 T).[35,36] The value of the MR becomes negative with the magnetic fields ranging from -6 T to 6 T when the temperature reaches 10 K. It indicates that the interfacial spin texture evolves due to the thermal effect. Impurity scattering dominates below 3 T, leading to a

reduction in MR. A butterfly-shaped hysteresis loop emerges in the MR at 50 K with the resistance peak at 2.5 T, which reflects the dynamic process of magnetic domain rearrangement. The R_{AHE} shown in Fig. 3(c) is obtained by subtracting the linear background from R_{xy}. The presence of disordered magnetic domains results in maximum scattering near the coercive field.[37] Meanwhile, the R_{AHE} exhibits a distinct hysteresis behavior, indicating the AHE in the CFO/Pt.

Figures 3(b) and 3(d) show the extracted MR at 6 T and R_{AHE} at different temperatures. The ΔMR decreases from 5 K to 20 K and increases when the temperature is higher than 20 K. The ΔR_{AHE} decreases from 6.04 mΩ to 3.93 mΩ. The temperature dependence of R_{AHE} originates from the competitive relationship between the MPE[38–41] and SHE.[12] These observations indicate that the temperature-mediated spin texture reconfiguration at the CFO/Pt interface leads to a transition in the MR from positive to negative values. Specifically, the competitive interplay between SMR and MPE in CFO/Pt at different temperatures modifies the spin texture,[42] thereby altering the transport behaviors of MR and R_{AHE}.

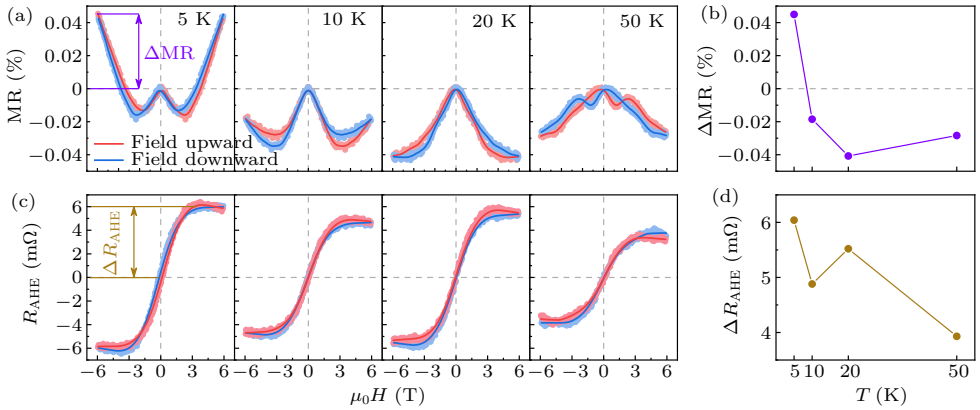


Fig. 3. Temperature-dependent magnetotransport measurements. (a), (c) The magnetoresistance and Hall resistance measured at 5 K, 10 K, 20 K and 50 K respectively. Red and blue circles represent the upward and downward scanning of magnetic field data, respectively (lines of corresponding colors represent the smoothing processing of the data). Notably, the R_{AHE} in (c) is derived by subtracting the linear background from R_{xy}. (b), (d) The amplitude of MR under 6 T (ΔMR) and R_{AHE} (ΔR_{AHE}) as a function of the temperature, respectively.

Although the low-temperature transport measurements indicate that MPE and SMR have the same origin of temperature-dependent MR and R_{AHE}, further experiments are still required to clarify their relationship at different temperature. This analysis is supported by the SMR:[43]

$$R_{xx} = R_0 + R_1 m_y^2, \tag{4}$$

$$R_{xy} = R_2 m_z + R_3 m_x m_y, \tag{5}$$

where $R_1 = -R_3$, and R_1/R_0 quantifies the SMR magnitude. R_2 incorporates contributions from both ordinary Hall effect (OHE) and Hall-type SMR, with $R_{2,\mathrm{OHE}}$ linearly dependent on $\mu_0 H$, yielding $R_2 = R_{2,\mathrm{SMR}} + R_{2,\mathrm{OHE}}(\mu_0 H)$. The angular dependence of the effect is governed by the magnetization projections m_x, m_y and m_z, where $m = M/M_{\mathrm{s}}$ denotes the unit vector of magnetization with M_{s} as the saturation magnetization.[43] In contrast, anisotropic magnetoresistance (AMR) in ferromagnetic metals follows the relationships[43]

$$R_{xx} = R_0 + \Delta R m_x^2, \tag{6}$$

$$R_{xy} = R_2 m_z + \Delta R m_x m_y, \tag{7}$$

where ΔR and R_2 arise from MPE. While SMR and AMR exhibit superficial similarities when magnetization is in-plane ($m_z = 0$), their angular dependencies differ fundamentally.[12] SMR arises when m rotates within the x–y plane (β-scans), driven by the reorientation of spin polarization; in contrast, AMR emerges during rotations within the x–z plane (γ-scans), which is attributed to symmetry-breaking SOC and magnetic order.[13] A critical distinction is that SMR vanishes when magnetization is out-of-plane ($m_z \neq 0$) during x–z plane rotations ($m_y = 0$), whereas AMR persists under the same x–z rotation conditions ($m_y = 0$). This difference enables clear experimental discrimination between the two effects.[36]

ADMR measurements are conducted on the CFO/Pt heterostructure at 10 K, 20 K and 50 K, respectively, with all tests carried out under an applied external magnetic field of 9 T (Fig. 4(a)). The results for the angle-dependent R_{xx} and R_{xy} are summarized in Figs. 4(b)–4(d). The relative resistance change with respect to angles β or γ is defined as $\Delta R/R = [R(\beta,\gamma) - R(0^\circ)]/R(0^\circ)$. Figure 4(b) shows the results of 360° rotations around the β and γ at 10 K. Notably, R_{xx} exhibits no angular dependence, whereas R_{xy} follows a sin β function with a 360° period, which is consistent with the AMR model described by Eqs. (6) and (7). Specifically, when the magnetic field rotates around the x-axis in the y–z plane, the magnetization component m_x equals 0. In Eq. (6), R_{xx} contains only a constant term. Hence, it lacks the angular dependence. While in Eq. (7), R_{xy} is solely associated with the m_z term (which scales with sin β). The curve's slight deviation from strict symmetry may arise from hysteresis induced by the sample rotation rate and angular offsets caused by sample inhomogeneity. For γ rotations at 10 K, R_{xx} follows a $\cos^2\gamma$

dependence with a 180° period (peaked at 90° and 270°), consistent with observations reported in other studies on CFO/Pt heterostructures;[23,24,36] R_{xy} meanwhile follows a $\cos\gamma$ dependence. These behaviors can also be derived from Eqs. (4) and (5): when the magnetic field rotates around the z-axis in the x–y plane, $m_z = 0$; Eq. (4) shows R_{xx} includes a constant term and an m_y^2 term (corresponding to $\cos^2\gamma$), while Eq. (5) indicates R_{xy} is proportional to $\cos\gamma$. Based on this analysis, AMR is determined to dominate at 10 K. Figure 4(c) shows the β- and γ-rotation results at 20 K: for β-rotations, R_{xx} follows a $\cos^2\beta$ dependence and R_{xy} follows a $\sin\beta$ dependence; for γ-rotations, R_{xx} exhibits no angular dependence and R_{xy} follows a $\cos\gamma$ dependence. These features align with the SMR model described by Eqs. (4) and (5), confirming SMR dominance at 20 K. Furthermore, ADMR results at 50 K are highly similar to those at 20 K, leading to the conclusion that as temperature increases, the contribution of SMR strengthens while that of AMR weakens. At lower temperatures, the MPE gradually increases, which can be attributed to enhanced exchange coupling between Fe^{3+} 3d orbitals and Pt 5d orbitals.[44] Combining with the temperature-dependent MR and R_{AHE} behaviors in Fig. 3, we speculate that SMR makes a greater contribution to MR, whereas MPE contributes more significantly to R_{AHE}. For quantitative analysis, we calculate the R_i parameters in Eqs. (4) and (5) using experimental data from Fig. 4. Following the calculations detailed in relevant references, the relative magnitude of the SMR effect is quantified by the ratios[43]

$$-\frac{R_1}{R_0} = \frac{\theta_{SH}^2 \left(2\lambda_{Pt}^2 \rho_{Pt}\right) (t_{Pt})^{-1} G_r \tanh^2\left(\frac{t_{Pt}}{2\lambda_{Pt}}\right)}{1 + 2\lambda_{Pt}\rho_{Pt} G_r \coth\left(\frac{t_{Pt}}{\lambda_{Pt}}\right)}, \tag{8}$$

where the spin Hall angle (θ_{SH}) is defined as the ratio of spin Hall conductivity (σ_{SH}) to electrical conductivity (σ), i.e., $\theta_{SH} = \sigma_{SH}/\sigma$. Additional key parameters are defined as follows: λ_{Pt} represents the spin diffusion length of Pt, ρ_{Pt} is the resistivity of Pt, t_{Pt} is the thickness of Pt layer, and G_r denotes the real part of the spin-mixing interface conductance $G_{\uparrow\downarrow}$. For calculations, we adopt the values $\theta_{SH} = 0.08$ and $\lambda_{Pt} = 2$ nm from previous studies, where the reported ρ_{Pt} values are of the same order of magnitude as those obtained in our work ($1 \sim 2 \times 10^{-7}$ Ω·m).[45,46] The R_1/R_0 ratios at 20 K and 50 K are 4×10^{-4} and 1.3×10^{-4}, respectively. Using Eq. (8), the G_r values at these temperatures are calculated to be 5.3×10^{14} and 1.4×10^{14} $\Omega^{-1}\cdot m^{-2}$, respectively.

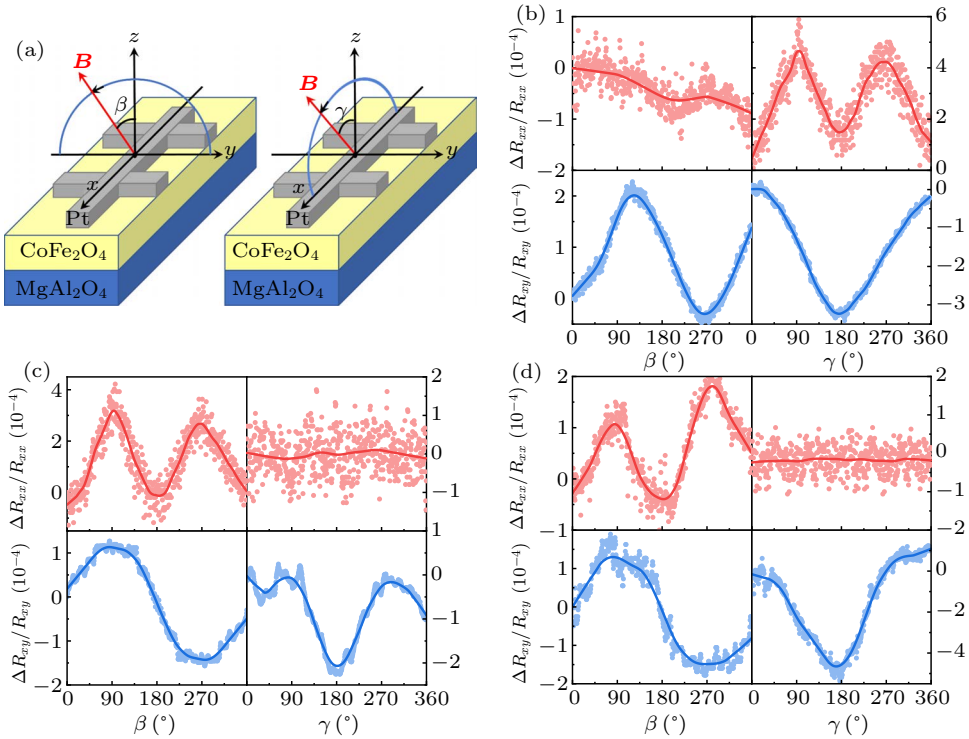


Fig. 4. (a) Measurement schematic diagram. Angular-dependent magnetoresistance measured at 10 K (b), 20 K (c) and 50 K (d), respectively. The red circles represent R_{xx} and the blue circles represent R_{xy} (lines of corresponding colors represent the smoothing processing of the data), which shows the variation of $\Delta R/R$ with the orientation of the external magnetic field when it rotates with respect to β and γ.

4. Conclusion

In summary, we have grown single-crystal CFO film and quantified the atomic magnetic moments in the film via XMCD spectroscopy. The results of magnetotransport measurement demonstrate that the value of the MR changes from the positive to negative when the temperature increases from 5 K to 10 K under high magnetic fields, and the R_{AHE} decreases as the temperature increases. Furthermore, the temperature-dependent ADMR indicates that the observed magnetotransport behaviors are ascribed to the competition between the MPE and SMR.

Acknowledgements

This work was supported by the National Natural Science Foundation of China (Grant Nos. 62525406, T2394473, 624B2070, and 62274085), the National Key Research and Development Program of China (Grant No. 2022YFA1402404), and the Innovation Program for Quantum Science and Technology of China (Grant No. 2024ZD0301300).

References

[1] Adachi H, Uchida K, Saitoh E and Maekawa S 2013 *Rep. Prog. Phys.* **76** 036501
[2] Manchon A, Zelezny J, Miron I M, Jungwirth T, Sinova J, Thiaville A, Garello K and Gambardella P 2019 *Rev. Mod. Phys.* **91** 035004
[3] Ando K, Takahashi S, Ieda J, Kajiwara Y, Nakayama H, Yoshino T, Harii K, Fujikawa Y, Matsuo M, Maekawa S and Saitoh E 2011 *J. Appl. Phys.* **109** 103913
[4] Vaz D C, Barthélémy A and Bibes M 2018 *Jpn. J. Appl. Phys.* **57** 0902A4
[5] Ando K, Takahashi S, Harii K, Sasage K, Ieda J, Maekawa S and Saitoh E 2008 *Phys. Rev. Lett.* **101** 036601
[6] Kimura T, Otani Y, Sato T, Takahashi S and Maekawa S 2007 *Phys. Rev. Lett.* **98** 156601
[7] Valenzuela S O and Tinkham M 2006 *Nature* **442** 176
[8] Hahn C, de Loubens G, Klein O, Viret M, Naletov V V and Ben Youssef J 2013 *Phys. Rev. B* **87** 174417
[9] Vlietstra N, Shan J, Castel V, Ben Youssef J, Bauer G E W and van Wees B J 2013 *Appl. Phys. Lett.* **103** 032401
[10] Vlietstra N, Shan J, Castel V, van Wees B J and Ben Youssef J 2013 *Phys. Rev. B* **87** 184421
[11] Vélez S, Bedoya-Pinto A, Yan W J, Hueso L E and Casanova F 2016 *Phys. Rev. B* **94** 174405
[12] Chen Y T, Takahashi S, Nakayama H, Althammer M, Goennenwein S T B, Saitoh E and Bauer G E W 2013 *Phys. Rev. B* **87** 144411
[13] Nakayama H, Althammer M, Chen Y T, Uchida K, Kajiwara Y, Kikuchi D, Ohtani T, Geprägs S, Opel M, Takahashi S, Gross R, Bauer G E W, Goennenwein S T B and Saitoh E 2013 *Phys. Rev. Lett.* **110** 206601
[14] Avci C O, Quindeau A, Pai C F, Mann M, Caretta L, Tang A S, Onbasli M C, Ross C A and Beach G S D 2017 *Nat. Mater.* **16** 309
[15] Wu H, Huang L, Fang C, Yang B S, Wan C H, Yu G Q, Feng J F, Wei H X and Han X F 2018 *Phys. Rev. Lett.* **120** 097205
[16] Yanagihara H, Uwabo K, Minagawa M, Kita E and Hirota N 2011 *J. Appl. Phys.* **109** 07C122
[17] Li Z L, Lyu Y, Ran Z, Wang Y J, Zhang Y, Lu N P, Wang M, Sassi M, Ha T D, N'Diaye A T, Shafer P, Pearce C, Rosso K, Arenholz E, Juang J Y, He Q, Chu Y H, Luo W D and Yu P 2023 *Adv. Funct. Mater.* **33** 2212298
[18] Moitra D, Hazra S, Ghosh B K, Jani R K, Patra M K, Vadera S R and Ghosh N N 2015 *RSC Adv.* **5** 51130
[19] Khan I and Hong J 2024 *J. Mater. Chem. C* **12** 17658
[20] Isasa M, Vélez S, Sagasta E, Bedoya-Pinto A, Dix N, Sánchez F, Hueso L E, Fontcuberta J and Casanova F 2016 *Phys. Rev. Appl.* **6** 034007
[21] Slonczewski J C 1958 *Phys. Rev.* **110** 1341
[22] Suzuki Y, vanDover R B, Gyorgy E M, Phillips J M, Korenivski V, Werder D J, Chen C H, Cava R J, Krajewski J J, Peck W F and Do K B 1996 *Appl. Phys. Lett.* **68** 714
[23] Isasa M, Bedoya-Pinto A, Vélez S, Golmar F, Sánchez F, Hueso L E, Fontcuberta J and Casanova F 2014 *Appl. Phys. Lett.* **105** 142402
[24] Tainosho T, Niizeki T, Inoue J, Sharmin S, Kita E and Yanagihara H 2017 *AIP Adv.* **7** 055936
[25] Collet M, Mattana R, Moussy J B, Ollefs K, Collin S, Deranlot C, Anane A, Cros V, Petroff F, Wilhelm F and Rogalev A 2017 *Appl. Phys. Lett.* **111** 202401
[26] Vasili H B, Gamino M, Gàzquez J, Sánchez F, Valvidares M, Gargiani P, Pellegrin E and Fontcuberta J 2018 *ACS Appl. Mater. Interfaces* **10** 12031
[27] Amamou W, Pinchuk I V, Trout A H, Williams R E A, Antolin N, Goad A, O'Hara D J, Ahmed A S, Windl W, McComb D W and Kawakami R K 2018 *Phys. Rev. Mater.* **2** 011401
[28] Peddis D, Cannas C, Piccaluga G, Agostinelli E and Fiorani D 2010 *Nanotechnology* **21** 125705
[29] Kim D H, Lee H J, Kim G, Koo Y S, Jung J H, Shin H J, Kim J Y and Kang J S 2009 *Phys. Rev. B* **79** 033402
[30] Kotani A 2008 *Phys. Rev. B* **78** 195115
[31] Chen J G 1997 *Surf. Sci. Rep.* **30** 1
[32] Chen C T, Idzerda Y U, Lin H J, Smith N V, Meigs G, Chaban E, Ho G H, Pellegrin E and Sette F 1995 *Phys. Rev. Lett.* **75** 152
[33] Wu R Q and Freeman A J 1994 *Phys. Rev. Lett.* **73** 1994
[34] Guo G Y, Ebert H, Temmerman W M and Durham P J 1994 *Phys. Rev. B* **50** 3861
[35] Wu H, Zhang Q, Wan C, Ali S S, Yuan Z, You L, Wang J, Choi Y S and Han X 2015 *IEEE Trans. Magn.* **51** 4100104
[36] Guo J Q, Meng K K, Zhang T Z, Liu J J, Chen J K, Wu Y, Xu X G and Jiang Y 2022 *Appl. Phys. Lett.* **121** 142403
[37] Xia T R, Yang X T, Zhang Y F, Liu X Q, Cai X Y, Liu C, Yao Q, Kou X F and Wang W B 2024 *Chin. Phys. B* **33** 087504
[38] Ding S L, Liang Z Y, Yun C, Wu R, Xue M Z, Lin Z C, Ross A, Becker S, Yang W Y, Ma X B, Chen D F, Sun K, Jakob G, Kläui M and Yang J B 2021 *Phys. Rev. B* **104** 224410
[39] Shao Q M, Grutter A, Liu Y W, Yu G Q, Yang C Y, Gilbert D A, Arenholz E, Shafer P, Che X Y, Tang C, Aldosary M, Navabi A, He Q L, Kirby B J, Shi J and Wang K L 2019 *Phys. Rev. B* **99** 104401
[40] Jin Q, Yang M, Song G Z, Zhao N, Chen S R, Hong H T, Cui T, Rong D K, Wang Q Y, Fan Y Y, Ge C, Wang C, Bi J C, Cao Y W, Wu L S, Wang S M, Jin K J, Cheng Z G and Guo E J 2024 *Chin. Phys. Lett.* **41** 027402
[41] Bai Y, Wang Z, Lei N, Muhammad W, Xiang L F, Li Q, Lai H L, Zhu Y Y, Wang W B, Guo H W, Yin L F, Wu R Q and Shen J 2022 *Chin. Phys. Lett.* **39** 108501
[42] Dong X J and Zhang C W 2024 *Chin. Phys. B* **33** 077303
[43] Althammer M, Meyer S, Nakayama H, *et al.* 2013 *Phys. Rev. B* **87** 224401
[44] Liang X, Zhu Y P, Peng B, Deng L J, Xie J L, Lu H P, Wu M Z and Bi L 2016 *ACS Appl. Mater. Interfaces* **8** 8175
[45] Hahn C, de Loubens G, Klein O, Viret M, Naletov V V and Ben Youssef J 2013 *Phys. Rev. B* **87** 174417
[46] Sagasta E, Omori Y, Isasa M, Gradhand M, Hueso L E, Niimi Y, Otani Y and Casanova F 2016 *Phys. Rev. B* **94** 060412